Journal of Alloys and Compounds 906 (2022) 164398

Contents lists available at ScienceDirect

Journal of Alloys and Compounds

journal homepage: www.elsevier.com/locate/jalcom

Modification of the thermometric performance of the lifetime-based luminescent thermometer exploiting Ti^{3+} emission in $SrTiO_3$ and $CaTiO_3$ by doping with lanthanide ions

W.M. Piotrowski[a], Z. Ristic[b], M.D. Dramićanin[b], Ł. Marciniak[a,*]

[a] Institute of Low Temperature and Structure Research, Polish Academy of Sciences, Okólna 2, Wroclaw 50-422, Poland
[b] Centre of Excellence for Photoconversion, Vinča Institute of Nuclear Sciences - National Institute of the Republic of Serbia, University of Belgrade, P.O. Box 522, Belgrade 11001, Serbia

ARTICLE INFO

Article history:
Received 6 January 2022
Received in revised form 22 February 2022
Accepted 27 February 2022
Available online 1 March 2022

Keywords:
Luminescent thermometry
Titanate
Perovskite
Charge difference
Ti^{3+} luminescence

ABSTRACT

Luminescence thermometry exploiting luminescence kinetics as a thermometric parameter is regarded as one of the most reliable temperature readout techniques. Transition metal ions are of particular interest in this application which is due to the possibility of modulating their spectroscopic properties by changing the strength of the crystal field of the matrix. In this work, we present a strategy to modulate the thermometric parameters including the relative sensitivity and useful temperature range of luminescent thermometers based on the lifetime of Ti^{3+} ions by introducing lanthanide (Ln^{3+}) doping in $SrTiO_3$ and $CaTiO_3$. The mutual effect of the distortion of the local symmetry of the Ti^{3+} ions associated with the introduction of Ln^{3+} ions and/or the $Ti^{3+} \rightarrow Ln^{3+}$ energy transfer enabled relative sensitivities of S_R = 5.87% K^{-1} at 140 K for $SrTiO_3$:Dy^{3+} and S_R = 4.51% K^{-1} at 251 K for $CaTiO_3$:Gd^{3+}.

1. Introduction

Inorganic phosphors doped with transition metal ions have attracted increasing interest as luminescent thermometers in recent years [1–6]. This is due to the strong differences in the electronic configurations of the $3d^n$ electronic levels on their ground and excited states, which entails a high susceptibility of their emission intensity to temperature changes and structural environment [7–10]. Taking advantage of these two features, the design of highly sensitive luminescent thermometers operating in any spectral range that can be easily modified by the crystal field engineering is possible [7,11,12]. Depending on the type of physical contact between the sensor and the measuring object, temperature sensors can be: (i) invasive, where the sensor is in direct contact (e.g., thermocouples); (ii) non-invasive, where there is no contact; and (iii) semi-invasive, in which the measured substance is altered to facilitate remote measurements [13–18]. In invasive temperature sensors, the single-spot readout mode causes perturbation of the temperature of the measured object, limits applications, and prevents thermal imaging of large surfaces or moving objects. Frequently, such sensors cannot be used in high electromagnetic fields, radioactive or corrosive environments. Non-invasive sensors, such as IR thermometers, require calibrations, they lack high spatial resolution and precision, and often require reflective properties of the substance prior to measurement [19]. Among the semi-invasive methods, temperature readouts using temperature induced changes in luminescence of the phosphor - luminescence thermometry - gained significant attention [20]. However, in order to facilitate the international development of a luminescent thermometer with on-demand modified parameters, a number of fundamental studies need to be carried out to understand the dependence and role of various mechanisms affecting luminescence and its variability as a function of temperature. The Ti^{3+} is a representative of transition metal ions having one of the simplest ($3d^1$) electronic configurations [21–23]. Its energy diagram consists only of a parabola of the ground level (for Ti^{3+} located in octahedral symmetry it will be $^2T_2$) and one excited level (in this case ^2E) [23]. The mutual position of these parabolas is strongly dependent on the crystal field and facilitates strong thermal quenching of Ti^{3+} luminescence. However, the number of studies devoted to its implementation in noncontact temperature sensing is very scanty [24–26]. Our recent studies reveal the high potential of Ti^{3+}, especially in lifetime-based thermometric approach, resulting in the highest relative sensitivity of this type of thermometer to date (8.83% K^{-1}) [26]. It has been found that the introduction of Ln^{3+}

* Corresponding author.
E-mail address: l.marciniak@intibs.pl (Ł. Marciniak).

https://doi.org/10.1016/j.jallcom.2022.164398
0925-8388/

dopant ions into $SrTiO_3$ causes the reduction of the titanium oxidation states from Ti^{4+} to Ti^{3+} through a charge compensation process. As a consequence, the luminescent properties of Ti^{3+} ions was significantly enhanced, which was manifested by an increase in the Ti^{3+} emission intensity and elongation of the lifetime of the Ti^{3+} excited state. The selection of the host material ($SrTiO_3$), which is characterized by relatively low crystal field strength (CFS) affecting the titanium ions, facilitates the occurrence of Ti^{3+} luminescence in the near infrared range. However, the main drawback of the obtained material was its extremely low operating temperature range of about 180 K. Therefore, in order to verify the possibility of modifying the thermometric performance of the Ti^{3+} lifetime-based thermometer, the effect of different types of Ln^{3+} ions on the spectroscopic properties of Ti^{3+} in $SrTiO_3$ should be compared. On the other hand, it can be expected that the consideration of another perovskite matrix, such as $CaTiO_3$, may shift the thermal operating range of the luminescent thermometer towards higher temperatures.

Therefore, in the present work, a systematic studies devoted to the evaluation of the modification of the thermometric properties of the lifetime-based luminescent thermometer exploiting Ti^{3+} emission in $SrTiO_3$ and $CaTiO_3$ host materials were investigated and discussed.

2. Experimental

The powders of $SrTiO_3$:1% Ln^{3+} and $CaTiO_3$:1% Ln^{3+} (where Ln^{3+} = Ce^{3+}, Pr^{3+}, Nd^{3+}, Sm^{3+}, Eu^{3+}, Gd^{3+}, Tb^{3+}, Dy^{3+}, Ho^{3+}, Er^{3+}, Tm^{3+}, Yb^{3+}) nanocrystals were synthesised by a modified Pechini method. The starting materials, which are given in Table S1, were used for the synthesis without further purification.

A stoichiometric amount of nitrates was dissolved in deionized water. In the case of Ln^{3+} co-doped nanocrystals, to obtain nitrates from oxides, their stoichiometric amounts were diluted in an aqueous solution of ultrapure nitric acid. Then, all the aqueous solutions of nitrates were mixed with a 6-fold stoichiometric excess of citric acid. Subsequently, an appropriate amount of $Ti(OC_4H_9)_4$ was mixed in a separate beaker with 2,4-pentanedione in a 1:1 molar ratio in order to stabilize the $Ti(OC_4H_9)_4$ solution. The contents of the beaker were gently stirred until a transparent, yellowish solution was obtained, which was then combined with the stabilized nitrate solution. Finally, PEG-200 was added to the mixture in 1:1 molar ratio with respect to citric acid. The resulting solutions were then dried for 3 days at 363 K until resins were formed. The produced resins of samples with 1% Ln^{3+} concentration relative to the number of moles of Sr^{2+} or Ca^{2+} ions were annealed in porcelain crucibles for 8 h in air at 1223 K. Finally, the obtained perovskite powders were grounded in an agate mortar.

All of the synthesized materials were examined by X-ray powder diffraction (XRPD) measurements carried out on a PANalitycal X'Pert diffractometer equipped with an Anton Paar TCU 1000 N temperature control unit, using Ni-filtered Cu-K_α radiation (V = 40 kV, I = 30 mA).

Transmission electron microscope (TEM) images were taken using a Philips CM-20 SuperTwin TEM microscope. The samples were dispersed in methanol, and a droplet of such suspension was put on a microscope copper grid. The samples were then dried and purified in a plasma cleaner. Studies were performed in a conventional TEM procedure with 160 kV parallel beam electron energy.

Emission spectra were measured using a 400 nm excitation line from a laser diode and a Silver-Nova Super Range TEC spectrometer from Stellarnet (1 nm spectral resolution) as a detector. Excitation spectra and luminescence decay profiles were recorded using the FLS1000 Fluorescence spectrometer from Edinburgh Instruments with an R928P side window photomultiplier tube from Hamamatsu as a detector with a 450 W halogen lamp and a 445 nm pulsed laser diode as the excitation sources. The temperature of the sample was controlled using a THMS 600 heating-cooling stage from Linkam (0.1 K temperature stability and 0.1 K set point resolution).

To obtain the results of relative sensitivity with lower uncertainty, all of the intensity vs temperature plots were fitted according to the Mott-Seitz equation (Eq. S2). The average lifetimes of excited states were determined from the double exponential fits of the emission decay profiles using (Eq. S3).

3. Results and discussion

3.1. Structural and morphological characterization

Although both strontium and calcium titanates belong to the same group of materials with the general chemical formula $A^{2+}B^{4+}O_3$, they represent different crystallographic systems [27–30]. $SrTiO_3$ at room temperature crystallizes in a cubic structure with *Pm-3 m* (221) space group and unit cell parameters: a_0 = 3.90528 Å, while $CaTiO_3$ under standard conditions crystallizes in an orthorhombic system with *Pbnm* (62) space group and lattice constants: a_0 = 5.40430 Å, b_0 = 5.42240 Å, c_0 = 7.65100 Å. When considering a_p as the unit cell parameter of the pseudo-cubic lattice for $CaTiO_3$ and the unit cell volume as $V = a_0 \cdot b_0 \cdot c_0 = \sqrt{2}a_p \cdot \sqrt{2}a_p \cdot 2a_p$, it can be concluded that a_p = 3.82704 Å takes a smaller value than the corresponding unit cell parameter a_0 for $SrTiO_3$ cubic lattice [31,32]. Both structures consist of 6-fold coordinated Ti^{4+} ion sites and Sr^{2+}/Ca^{2+} ions surrounded by 12 oxygen atoms creating cuboctahedra (Fig. 1a-b). However, in the case of the $SrTiO_3$ structure (Z = 1), Sr^{2+} ions are located in the center of the unit cell with equally distant Ti^{4+} ions, while the distortion of Ca^{2+} cuboctahedra in $CaTiO_3$ (Z = 4) generates the occurrence of non-equivalent Ca^{2+}-Ti^{4+} distances. As a result, the $(TiO_{12})^{20-}$ cuboctahedra in the $CaTiO_3$ structure are distorted and thus three different Ti^{4+}-O^{2-} distances ($R(Ti^{4+}\text{-}O_{(1)}{}^{2-})$ = 1.94620 Å; $R(Ti^{4+}\text{-}O_{(2)}{}^{2-})$ = 1.95134 Å; $R(Ti^{4+}\text{-}O_{(2)}{}^{2-})$ = 1.96071 Å) are present. It should be noted that $O_{(2)}{}^{2-}$ are oxygen ions localized between two Ti^{4+} for which the metal-oxygen interaction is unequal and therefore two values of $R(Ti^{4+}\text{-}O_2{}^{2-})$ can be distinguished around one Ti^{4+} ion [33]. The shortest Ti^{4+}-O^{2-} for $CaTiO_3$ is shorter than the counterpart found for $SrTiO_3$ ($R(Ti^{4+}\text{-}O^{2-})$ = 1.95264 Å), which may indicate that the stronger crystal field strength affects the titanium ions in the $CaTiO_3$ structure.

When doping both matrices with Ln^{3+} ions, due to the small difference in ionic radii, A^{2+} (Sr^{2+}/Ca^{2+}) crystallographic sites (Shannon ionic radii equals 144 pm for Sr^{2+} and 134 pm for Ca^{2+}) are expected to be more suitable for substitution by Ln^{3+} ions (effective radii maintain in the range between 134 pm for 12-fold coordinated Ce^{3+} and 98.5 pm for 8-fold coordinated Yb^{3+}) compared to Ti^{4+} sites (effective ionic radius equals 60.5 pm). However, the charge difference between Sr^{2+}/Ca^{2+} and Ln^{3+} ions is noteworthy. As reported previously for the $SrTiO_3$ structure, the incorporated Ln^{3+} ions embedded in A^{2+} sites result in the stabilization of 6-fold coordinated Ti^{3+} centers adjacent to Ln^{3+} polyhedrons related to []–Ti^{3+}–O oxygen vacancies (where [] is an oxygen vacancy) [26,34]. Additionally, the introduction of Ln^{3+} ions leads to a change of the Goldschmidt tolerance factor *t*, which describes the degree of distortion from ideal cubic symmetry of perovskite structures (Eq. S1) [27,35]. As shown in Fig. 1c, for the $SrTiO_3$ cubic structure $t \approx 1$, while lower t values can be found for $CaTiO_3$, which stays in agreement with the results found in the literature [33,36,37]. The incorporation of Ln^{3+} ions leads to obtaining a lower value of the Goldschmidt criterion, especially when the atomic number increases and the ionic radius of Ln^{3+} ions in the same coordination decreases (so-called lanthanide contraction).

To verify the crystallographic purity of the prepared nanomaterials [38,39], X-ray powder diffraction (XRPD) measurements were conducted at room temperature and the obtained patterns were

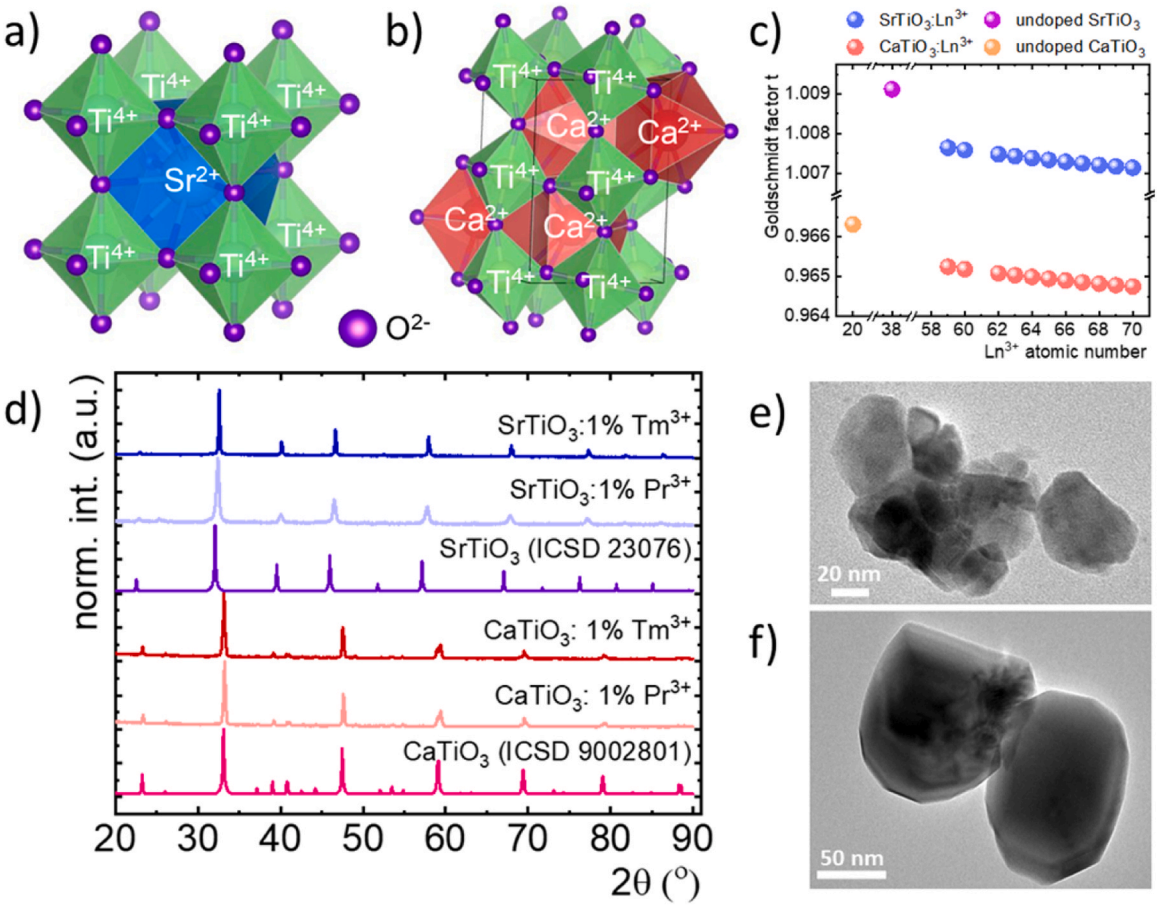

Fig. 1. Structural characterization of the synthesized materials: visualization of Ti^{4+} and Sr^{2+}/Ca^{2+} polyhedra in $SrTiO_3$ – (a) and $CaTiO_3$ structures – (b); dependence of the Goldschmidt tolerance factor as a function of the Ln^{3+} atomic number in $SrTiO_3$:1% Ln^{3+} and $CaTiO_3$:1% Ln^{3+} – (c); X-ray diffraction patterns of representative $SrTiO_3$:1% Ln^{3+} and $CaTiO_3$:1% Ln^{3+} powders – (d); representative TEM images of $SrTiO_3$:Pr^{3+} – (e) and $CaTiO_3$:Pr^{3+} (f) nanocrystals –.

compared with the reference data (Fig. 1d, see also Figs. S1-S2). Independently of Ln^{3+} doping in both $SrTiO_3$ and $CaTiO_3$ structures, no additional reflections in the diffraction pattern were observed. Additionally, an increase in unit cell volume with increasing Goldschmidt tolerance factor was noted (Fig. S3). This is due to the fact that as the ionic radius of the dopant increases, the unit cell gradually expands. It can also be clearly confirmed by the observed shift of peak positions towards higher angles when substituting Sr^{2+} ions with smaller Pr^{3+} and even smaller Tm^{3+} ions in $SrTiO_3$:Ln^{3+} materials (Fig. 1d). For $CaTiO_3$:Ln^{3+} this effect is also noticeable, but is not as spectacular due to the smaller difference between the sizes of Ca^{2+} and Ln^{3+} ions. Moreover, the influence of the matrix on the morphology of the obtained nanocrystals was confirmed by transmission electron microscopy (TEM) measurements. Representative TEM images of $SrTiO_3$:Pr^{3+} and $CaTiO_3$:Pr^{3+} are presented in Fig. 1e, f (see more in Figs. S4, S5). In general, the synthesized materials are well crystallized. It was found that for $CaTiO_3$ the grains are better separated in respect to $SrTiO_3$, but in both cases the nanocrystals do not form excessive aggregates. Taking advantage of the Feret method, the particle size distribution for both perovskite lattices was determined (Fig. S6). The above mentioned difference in aggregation can probably be combined with the contrasting values of the average grain size, which for $SrTiO_3$ equals 39.0 nm while for $CaTiO_3$ – 132.2 nm.

To develop a luminescent thermometer with predefined and predictable thermometric properties, thermally induced structural changes should be understood. In the case of $SrTiO_3$ lattice, Tsunekawa et al. reported that the positive thermal expansion coefficient α increases with temperature [40]. It is noteworthy that initially the increase of α is quasi-linear up to a temperature of about 80 K, where it reaches a value of about $0.8{\cdot}10^{-5}$ K^{-1}, then gradually increases to $1{\cdot}10^{-5}$ K^{-1} at 110 K, after which it falls sharply to $0.6{\cdot}10^{-5}$ K^{-1} and remains almost constant at higher temperatures. The abrupt change in the thermal expansion coefficient is due to the phase transition between tetragonal (*I4/mcm*) and cubic (*Pm-3 m*) symmetry. Ab initio calculations estimated the critical temperature T_c of the phase transition to be around T_c = 80 K [41], while experimental data from inelastic neutron scattering and Raman spectroscopy for single-crystal strontium titanate confirms that it undergoes a phase transition at 108–110 K [42–45]. Therefore, to verify whether a similar phase transition would be observed for nanocrystals, Raman spectra were measured for a representative $SrTiO_3$:Gd^{3+} sample as a function of temperature (Fig. S8). Similar to bulk $SrTiO_3$, broad bands with the maxima at 265 and 679 cm^{-1} are observed, which is due to the second order features of cubic centrosymmetric $SrTiO_3$. All of the 12 zone-center optical phonons should be inactive in first-order Raman scattering because they are of an odd parity with respect to the inversion [46]. However, for the synthesized $SrTiO_3$ nanocrystals, several aspects can result in a breakdown of the inversion symmetry selection rules, e.g. the oxygen vacancies induced by Ti^{3+} charge compensation and surface defects [47]. Therefore, the decrease of the crystal symmetry leads to the appearance of first-order scattering bands centered at 143, 171, 265, 545 and 796 cm^{-1}, corresponding to TO_1, TO_2 +LO_1, TO_3, TO_4 and LO_4 modes, respectively (where LO and TO correspond to longitudinal and transverse optical phonons, respectively). Over the temperature range studied, all bands were quenched at different temperatures, except for the TO_2 +LO_1 hard mode. Therefore, TO_1 as a soft mode was quenched at

173 K; TO_3 at 263 K; TO_4 above 400 K, and LO_4 almost completely quenched at 473 K. On the other hand, in the case of $CaTiO_3$ materials, phase transitions have been reported over a range of much higher temperatures compared to $SrTiO_3$ [28,31,32]. High-temperature neutron and X-ray powder diffraction measurements conducted by Redfern [48] and notwithstanding by Kennedy et al. [49] demonstrated a structural phase transition of $CaTiO_3$ from orthorhombic (*Pbnm*) to tetragonal (*I4/mcm*) symmetry at 1373 K, while Ali and Yashima [32] referred that the $CaTiO_3$ orthorhombic structure maintains to 1486 K. Moreover, Gränicher and Jakits [50] declared that no phase transition below room temperature was observed for pure-phased $CaTiO_3$. Nevertheless, according to ab-initio calculations, different sources give a thermal expansion coefficient α increasing with temperature from $\alpha = 1.5{\cdot}10^{-5}$ K^{-1} at 100 K to $3.2{\cdot}10^{-5}$ K^{-1} or $4.0{\cdot}10^{-5}$ K^{-1} at 200 K [29,51]. Finally, experimental measurements of Knight [52] showed that the $CaTiO_3$ cell volume increases and reaches the values 222.6, 223.1 and 223.7 A^3 when the temperature elevates successively from 100, 200–300 K. To evaluate if investigated $CaTiO_3$ nanocrystals perform similar thermally dependent structural properties, thermal evolution of Raman spectra for $CaTiO_3$:Gd^{3+} was carried out (Fig. S9). In contrast to $SrTiO_3$, it should be expected that several optical vibrational modes are Raman-active for $CaTiO_3$ which belongs to the orthorhombic system with lower symmetry [53]. Indeed, the Raman spectra consist of multiple bands, one of which, with a maximum at 150 cm^{-1}, can be assigned to the Ca–TiO_3 lattice vibration mode; 183, 229, 251, 289 and 341 cm^{-1} to the O–Ti–O bending vibration modes; 471 and 495 cm^{-1} as the Ti-O_3 torsional modes (bending or internal vibration of oxygen cage) and 617 and 799 cm^{-1} as the Ti–O symmetric stretching vibration modes (LO_3) [54,55]. Moreover, it is noteworthy that the peak at 183 cm^{-1} is also correlated to the motion of the A-site (Ca^{2+}) ions (TO_2 + LO_1). The frequencies of most of the band centres decrease with increasing temperature. Among the mentioned O–Ti–O bending modes, the greatest changes of Raman shift are observed between 251.6 and 239.1 cm^{-1} (12.5 cm^{-1}) in the temperature range from 83 to 573 K (see Fig. S9b).

3.2. Luminescent properties characterization

In the case of the absorption spectra of Ti^{4+} based host materials, i.e. $SrTiO_3$ and $CaTiO_3$, the broad band associated with the O^{2-}→Ti^{4+} charge transfer transition is expected to occur at the short wavelength part of spectra. Opposite transfer of electron may result in the occurrence of Ti^{4+}→ O^{2-} charge transfer emission band, but this process is not expected to be efficient. However, as presented in previous work in the case of $SrTiO_3$ nanoparticles, doping with non-luminescent lanthanide ions (La^{3+} and Lu^{3+}), which substitute Sr^{2+}, results in the reduction of titanium ions and stabilization of Ti^{3+} oxidation state [26]. Therefore, when considering the spectroscopic properties of $SrTiO_3$:Ln^{3+} and $CaTiO_3$:Ln^{3+} compounds, the energy diagram of Ti^{3+} ions of $3d^1$ electronic configuration should be studied (Fig. 2a). In both cases electrons can be efficiently transferred from the ground $^2T_2$ state to the excited ^2E state by λ_{exc} = 400 nm. This is followed by a nonradiative relaxation to the bottom of the ^2E parabola, from which the electrons return to the ground level with the occurrence of emission in the deep red spectral range. However, in the local point symmetry, distorted with respect to the octahedral symmetry, both ^2E and $^2T_2$ states of Ti^{3+} can be split [23]. The difference in the crystal field strength affecting the Ti^{3+} ions results in the difference in the shape of the excitation and emission bands of Ti^{3+} in $SrTiO_3$ and $CaTiO_3$ nanocrystals. For the low temperature excitation spectrum of representative $SrTiO_3$ doped with Gd^{3+} ions, two spectrally overlapping bands can be distinguished (Fig. 2b). The broader and more intense band of lower energy (with the maximum at around 24,400 cm^{-1}, 410 nm) corresponds to the $^2T_2$→^2E transition of Ti^{3+} ions, while the second band (with the center at ~26600 cm^{-1}, 375 nm) is related to the above mentioned O^{2-}→Ti^{4+} charge transfer transition. The excitation spectra for the other $SrTiO_3$:Ln^{3+} samples reveal that the bands are in a similar range (Fig. S9). However, it should be mentioned that among the optically active lanthanides, no excitation bands for Ti^{3+} ion emission could be recorded for $SrTiO_3$:Ce^{3+} and $SrTiO_3$:Eu^{3+}. This may suggest that in the case of the $SrTiO_3$:Ce^{3+} synthesis, cerium ions are embedded in the octahedral Ti^{4+} site, which is favorable for Ce^{4+} charge, preventing the generation of Ti^{3+} ions. For $SrTiO_3$:Eu^{3+} such a result could be also expected due to the 2 + oxidation state favored by Sr^{2+} ions instead of 3 + for Eu ions. On the other hand, in $CaTiO_3$:Gd^{3+} nanocrystals, a shift of both excitation bands towards higher energies in respect to the $SrTiO_3$:Gd^{3+} counterpart was observed with maxima at 29,850 cm^{-1} (335 nm) and ~24700 cm^{-1} (405 nm) for the O^{2-} →Ti^{4+} charge transfer and $^2T_2$→^2E transitions, respectively (Fig. S10). It can be concluded that this is related to the shorter metal-ligand distance $R_{min}(Ti^{4+}\text{-}O^{2-})$, compared to the distance in the $SrTiO_3$ structure, and the well-known relationship between 10Dq crystal field strength and R, originally proposed by Tanabe and Sugano [56,57] as follows:

$$10Dq = \frac{A}{R^n} \quad (1)$$

where A is a constant and n depends on covalent and exchange effects and can vary from 3.5 to 7.3 for different systems [58]. In the case of calcium titanate doped with Ce^{3+} ions, the lack of excitation bands of Ti^{3+} ions was observed again. However, contrary to the $SrTiO_3$:Eu^{3+}, the emission and excitation bands of Ti^{3+} ions in $CaTiO_3$:Eu^{3+} were observed. It was found that decreasing ionic radius of the lanthanides from Nd^{3+} to Yb^{3+} results in a shift of the centre of the Ti^{4+} charge transfer band by 500 cm^{-1} from 29,600 cm^{-1} (338 nm) to 30,100 cm^{-1} (332.5 nm). On the other hand, the smooth redshift of the Ti^{3+} excitation band maximum from 25,600 cm^{-1} (390 nm) to 24,300 cm^{-1} (411 nm) can be observed. These effects can be explained in terms of an increase in the average Ti^{3+} to O^{2-} distance, which results in a lowering of the crystal field strength affecting the Ti^{3+}. Simultaneously, an increase in the interionic distance results in an increase of the energy which needs to be provided to transfer an electron between O^{2-} and Ti^{4+} The difference in the shape of the emission band of Ti^{3+} ions is well illustrated by comparing the emission spectra of representative $SrTiO_3$:Gd^{3+} and $CaTiO_3$:Gd^{3+} (Fig. 2c). Bearing in mind that the Tanabe Sugano diagram for ions with $3d^1$ configuration consists only of a $^2T_2$ ground and ^2E excited state, the bands with maxima at 791 nm and 770 nm for $SrTiO_3$ and $CaTiO_3$, respectively, with the subsequent broad bands, should be considered as ^2E Stokes-like phonon sidebands induced by lattice vibrations. The occurrence of a much broader emission band of Ti^{3+} ions observed in $CaTiO_3$ results from a stronger distortion of the Ti^{3+} site from octahedral symmetry and thus a stronger splitting of the emitting ^2E state [28].

The intersection of the ground ^2E and excited $^2T_2$ level parabolas of Ti^{3+} leads to the possibility of the occurrence of nonradiative thermal quenching of the excited state population at elevated temperatures, which enables the development of a luminescent thermometer. As already shown, the introduction of Ln^{3+} ions leads to a modification of the crystal field strength affecting the Ti^{3+} ions, which may additionally modify the activation energy of the thermal quenching of Ti^{3+} emission intensity. To verify this hypothesis, the thermal evolution of the emission spectra of $SrTiO_3$ and $CaTiO_3$ doped with different Ln^{3+} ions was evaluated (Fig. 3a and b; all other emission spectra are presented in Fig. S13 and Fig. S14). It may be noted that at elevated temperatures the intensity of the Ti^{3+} emission band decreases without any evidence of its spectral shift for both host materials. It can be found that the emission intensity of Ti^{3+} in $SrTiO_3$:Ln^{3+} materials starts to be quenched already above 123 K, while for $CaTiO_3$:Ln^{3+} nanocrystals the thermal quenching process becomes evident above 160 K (Fig. 3c and d). Additionally, in

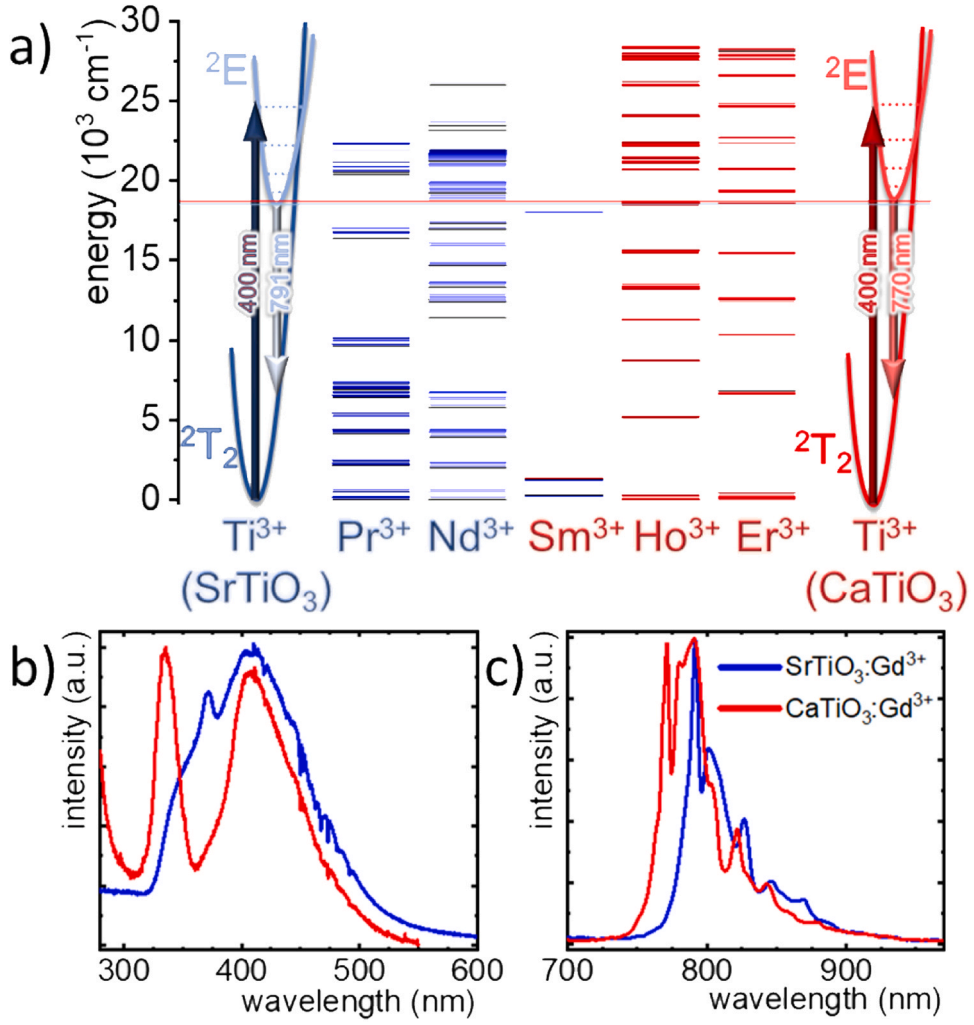

Fig. 2. Simplified energy diagrams of representative Ln^{3+} ions and configurational coordinate diagram of Ti^{3+} ions in $SrTiO_3$ and $CaTiO_3$ – a); comparison of excitation spectra (λ_{em} = 791.5 nm for $SrTiO_3$:Gd^{3+} and λ_{em} = 770 nm for $CaTiO_3$:Gd^{3+}) – b) and emission spectra (λ_{exc} = 400 nm,) measured at 83 K for $SrTiO_3$:Gd^{3+} and $CaTiO_3$:Gd^{3+} – c.

the case of $CaTiO_3$:Ln^{3+} nanocrystals in the low temperature range, an increase in temperature results in the enhancement of the emission intensity. The enhancement rate depends on the Ln^{3+} ion and was found to be the strongest for $CaTiO_3$:Tb^{3+}, for which intensity reached 178% at 183 K of its initial emission intensity. This effect can be explained in terms of an increase in the absorption cross section at 400 nm at elevated temperature, caused by the thermally induced broadening of the excitation band. Since in the case of smaller Ln^{3+} ions the spectral position of excitation bands is red-shifted, the excitation line of 400 nm is mismatched with the excitation band maxima to the higher extent. Hence the enhancement effect is the strongest in this case. The higher quenching temperature observed in the case of $CaTiO_3$:Ln^{3+} results from the higher activation energy of the nonradiative depopulation of the Ti^{3+} excited state, which is a consequence of the higher crystal field strength. A second possible explanation of this process is the thermal dependence of the probability of the $^2E \rightarrow {}^2T_2$ electronic transition, which will be discussed in the latter part of this manuscript. It is noteworthy that the type of Ln^{3+} dopant ion affects the thermal quenching rate of Ti^{3+} intensity. However, systematic studies are difficult here since several processes and effects occur simultaneously: a change in the local ions symmetry related to the introduction of Ln^{3+} into the Sr^{2+} site and the occurrence of 4 f energy levels of Ln^{3+} ions, which enables the $Ti^{3+} \rightarrow Ln^{3+}$ energy transfers. The confirmation of the later process is the occurrence of additional emission bands in the spectra of $SrTiO_3$:Ln^{3+} and $CaTiO_3$:Ln^{3+} associated with *4–4 f* electronic transitions of Ln^{3+} ions. As mentioned above, in the case of Eu^{3+} doped samples, weak Ti^{3+} emission is observed only for $CaTiO_3$:Eu^{3+}. Nevertheless, emission of Eu^{3+} ions with the maxima at around 594, 617, 654 and 697/705 nm correlated with $^5D_0 \rightarrow {}^7F_J$ transitions (where J = 1, 2, 3, 4) was measured in the cases of both lattices. On the other hand, the partial overlap of the $^4F_{5/2} \rightarrow {}^4I_{9/2}$ (with a maximum at 808 nm) and $^4F_{9/2} \rightarrow {}^6H_{9/2}$ bands (at around 755 nm) of Nd^{3+} and Dy^{3+}, respectively may slightly affect further analysis. Unfortunately, analysis of the thermal quenching of Ti^{3+} emission bands for $SrTiO_3$:Tm^{3+} and $CaTiO_3$:Tm^{3+} samples is not possible due to the spectral overlap of the intense $^3H_4 \rightarrow {}^3H_6$ band (at about 800 nm) with the $^2E \rightarrow {}^2T_2$ band of Ti^{3+} ions. Nevertheless, the thermal dependence of the intensity vs temperature plot is similar for all $CaTiO_3$:Ln^{3+} dopant ions and an increase in intensity at low temperatures, followed by a gradual decrease until complete quenching can be found. On the other hand, the initial increase in emission intensity for $SrTiO_3$:Ln^{3+} occurs only for Ln^{3+} =Pr^{3+}, Nd^{3+}, Tb^{3+}, Ho^{3+} and Yb^{3+}. The highest intensity increase (of 111%) was obtained at T = 133 K for $SrTiO_3$:Nd^{3+} nanopowder. All the studied $CaTiO_3$:Ln^{3+} nanocrystals except $CaTiO_3$:Dy^{3+} are characterized by a more significant growth of $^2E \rightarrow {}^2T_2$ band intensity compared to $SrTiO_3$:Ln^{3+} samples. It is also worth noting that higher temperatures above which thermal quenching of Ti^{3+} emission intensity was found for $CaTiO_3$:Ln^{3+} with respect to the

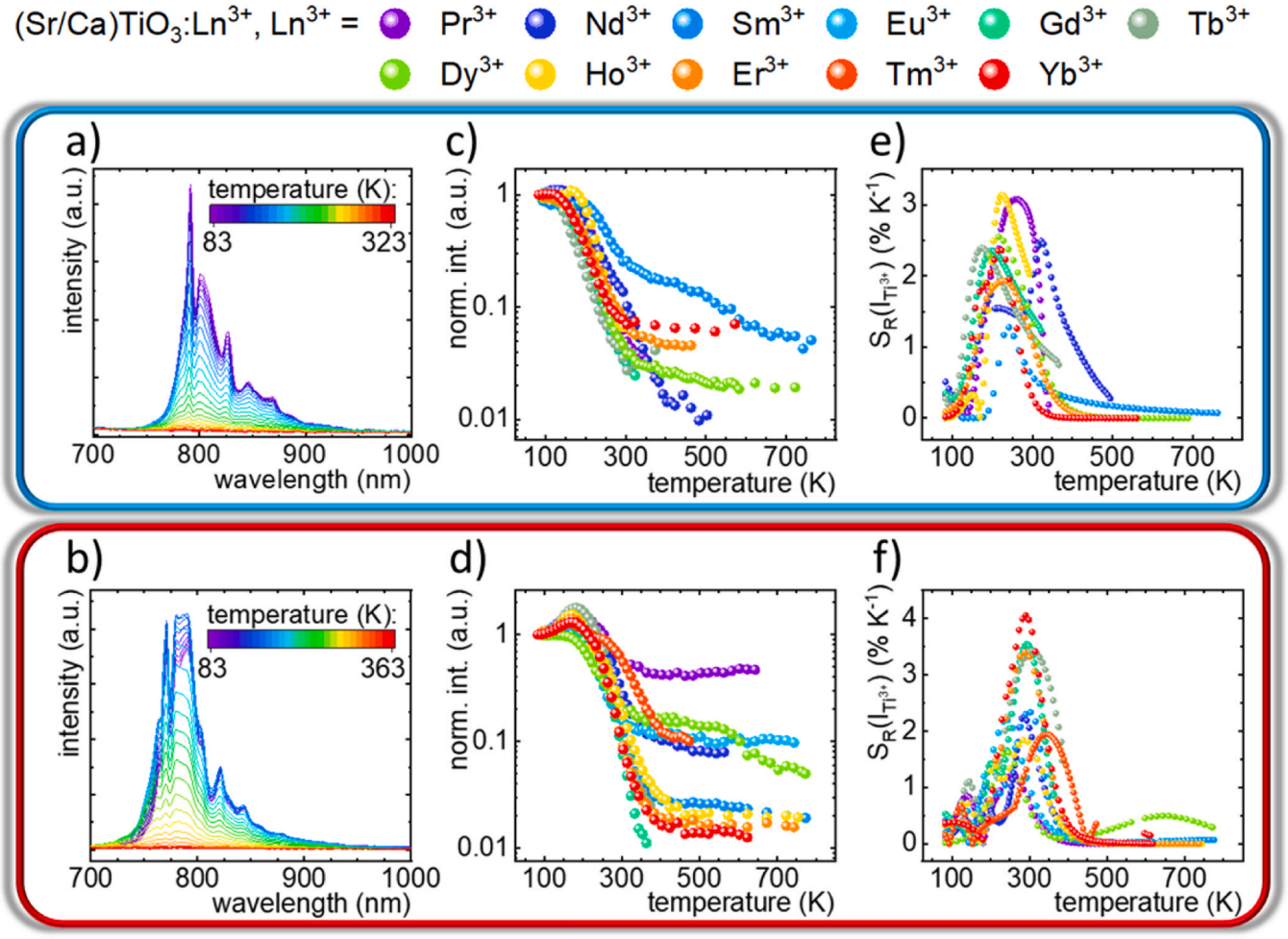

Fig. 3. Representative thermal evolution of emission spectra for $SrTiO_3:Gd^{3+}$ – (a) and $CaTiO_3:Gd^{3+}$ – (b); thermal evolution of intensity of Ti^{3+} emission band I_{Ti3+} (c, d) and relative sensitivities $S_R(I_{Ti3+})$ (e, f) calculated for $SrTiO_3:Ln^{3+}$ (c, e) and $CaTiO_3:Ln^{3+}$ (d, f).

$SrTiO_3:Ln^{3+}$. A commonly used parameter to quantify the rate of thermal quenching of luminescence is $T_{1/2}$ defined as the temperature at which the emission intensity reaches 50% of the initial value. This parameter also confirms that for all $SrTiO_3:Ln^{3+}$ compounds the thermal quenching process occurs at lower temperatures ($T_{1/2}$ = 196 K) than for $CaTiO_3:Ln^{3+}$ ($T_{1/2}$ = 265 K). These parameters stay in agreement with the expected results, due to the mentioned difference in the CFS value and the linear relationship between CFS and the distance between the ground $^2T_2$ and excited ^2E levels of Ti^{3+} ions. To quantitatively verify the influence of structure on the thermal changes of Ti^{3+} luminescence, the absolute S_A and relative S_R sensitivities were calculated according to the following formulas:

$$S_A = \left|\frac{\Delta\Omega}{\Delta T}\right| \cdot 100\% \quad (2)$$

$$S_R = \left|\frac{1}{\Omega}\frac{\Delta\Omega}{\Delta T}\right| \cdot 100\% \quad (3)$$

where Ω is the thermometric parameter (in this case I_{Ti3+}) and ΔΩ represents its change for a ΔT change of temperature. The thermal evolutions of the absolute sensitivity are plotted in Figs. S16 and S17, and of relative sensitivity in Figs. 3e and 3f (see also the comparison of maximal values of S_A and S_R in Table S2). The highest maxima of S_A values were obtained for $CaTiO_3:Tb^{3+}$ and $SrTiO_3:Ho^{3+}$ (S_{Amax} = 20.14 and 17.99 · 10^{-3} K^{-1}, respectively). It was found that most of the S_A values obtained can be correlated with the probability of energy transfer occurring between Ti^{3+} and Ln^{3+} ions (Fig. 2a and Fig. S18). High values of S_{Amax} (above 10 · 10^{-3} K^{-1}) can be attributed to both $SrTiO_3$ and $CaTiO_3$ doped with Pr^{3+}, Nd^{3+}, Eu^{3+}, Tb^{3+}, Ho^{3+} and Er^{3+} ions. It is not clear why relatively high S_{Amax} values were obtained for Yb^{3+} and Gd^{3+} ions (11.59, 16.17, 10.25 and 13.8 · 10^{-3} K^{-1} for $SrTiO_3:Yb^{3+}$, $CaTiO_3:Yb^{3+}$, $SrTiO_3:Gd^{3+}$ and $CaTiO_3:Gd^{3+}$, respectively), which have energy levels located far away from the ^2E excited state of Ti^{3+} (the energy gap from $^2F_{5/2}$ of Yb^{3+} is bigger than 8000 cm^{-1}). In this case, the highest S_{Rmax} values were calculated as follows: S_{Rmax} = 3.08% K^{-1} at 258 K for $SrTiO_3:Pr^{3+}$, S_{Rmax} = 3.14% K^{-1} at 224 K for $SrTiO_3:Ho^{3+}$, S_{Rmax} = 3.55% K^{-1} at 295 K for $CaTiO_3:Gd^{3+}$ and S_{Rmax} = 4.47% K^{-1} at 393 K for $CaTiO_3:Yb^{3+}$. Another important parameter that can be used to describe the utility of a luminescent thermometer is the temperature range over which it is sufficiently sensitive (S_R > 1% K^{-1}) [59]. Therefore, it is worth noting that a significant proportion of the investigated thermometers based on Ti^{3+} ions emission offer high sensitivity in the physiological temperature range. This temperature range exceed 200 K for $SrTiO_3:Nd^{3+}$ (163–413 K) and for $CaTiO_3:Tm^{3+}$ (377–413 K). However, the widest range was found in $CaTiO_3:Yb^{3+}$, for which S_R > 1% K^{-1} remains in temperature range as wide as over 350 K (207–563 K). Despite the obtained high sensitivity values for thermometers based on single band emission, such thermometers cannot be applied for reliable temperature determination since the intensity of a single emission band may be affected by many additional processes, like excitation intensity, concentration of phosphor, etc. Nevertheless, such an investigation enables qualitative analysis of thermal quenching rates,

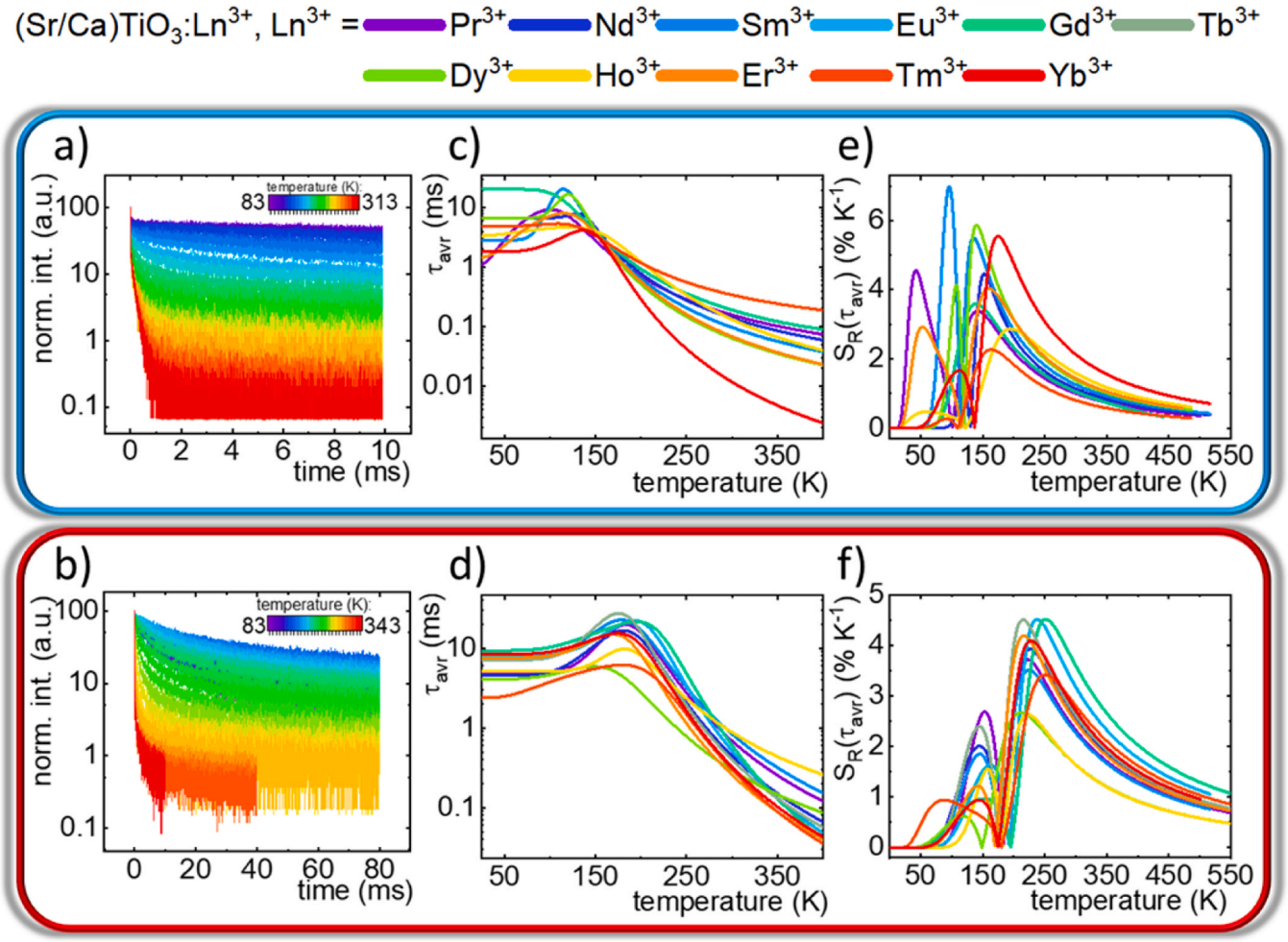

Fig. 4. The representative thermal evolution of luminescent decays for $SrTiO_3:Er^{3+}$ – (a) and $CaTiO_3:Sm^{3+}$ – (b); thermal evolution of average decays τ_{avr} (c, d) and the relative sensitivities $S_R(\tau_{avr})$ (e, f) calculated for $SrTiO_3:Ln^{3+}$ (c, e) and $CaTiO_3:Ln^{3+}$ (d, f).

which is important for the development of highly sensitive luminescent thermometers.

In contrary to the emission intensity of a single band, the lifetime of the excited state of emitting ions is considered as the most reliable thermometric parameter due to the fact that the analysis of the kinetics of the luminescence provides almost complete independence of its decay on the scattering or absorption of the light emitted by the medium. Therefore, a temperature series of luminescent decay measurements were carried out for Ln^{3+}-doped $SrTiO_3$ and $CaTiO_3$ nanocrystals (Fig. 4a and b; see more in Figs. S19, S20). Due to the nonexponential decay observed for measurements performed at higher temperatures, the average lifetimes (τ_{avr}) were calculated according to the methodology described in the experimental section. Analogously to the Ti^{3+} emission intensity, at low temperatures the lifetime of the ^2E state elongates with temperature rise. The maximal values of τ_{avr} were found at around 140 K for $SrTiO_3:Ln^{3+}$ and at around 183 K for $CaTiO_3:Ln^{3+}$. The effect of elongation of the τ_{avr} at elevated temperature is unusual, however has been observed in the case of other transition metal ions such as Cr^{3+} and Mn^{4+} and has been discussed as a relaxation of the selection rules associated with thermally induced mixing of the wavefunctions of excited states [8,60,61]. In such a case, the electronic transition of Ti^{3+} becomes more allowed, leading to an increase in the probability of the $^2E \rightarrow {}^2T_2$ radiative transition. The correlation between the elongation of the τ_{avr} and the increase in emission intensity at elevated temperatures provides evidence that the main process responsible for both effects is a thermally induced change in the probability of the radiative electronic transition in Ti^{3+} ions. The most spectacular elongation of τ_{avr} was observed for $SrTiO_3:Nd^{3+}$, for which the average lifetime τ_{avr} increased from 4.2 ms at 83 K to as much as 20.7 ms at 115 K, i.e. almost 500% of the initial value, while for $CaTiO_3:Ln^{3+}$ the largest variation was obtained for $CaTiO_3:Tb^{3+}$, with an almost fourfold elongation from τ_{avr} = 7.2 ms at 83 K to 27.5 ms at 175 K. It is worth to notice that the effect of τ_{avr} elongation was not observed only in the case of $SrTiO_3:Gd^{3+}$, $SrTiO_3:Ho^{3+}$ and $SrTiO_3:Tm^{3+}$. The fact that τ_{avr} elongation was observed for all Ln^{3+} in $CaTiO_3:Ln^{3+}$ suggests that this host material is especially sensitive to the change of the probability of $^2E \rightarrow {}^2T_2$ electronic transition due to the stronger initial distortion from the octahedral symmetry of Ti^{3+} and due to the larger difference in ionic radii between Ln^{3+} and Ca^{2+}, which further enhances this distortion. The differences in the thermal shortening rates of Ti^{3+} lifetime after introducing Ln^{3+} ions is associated with the $Ti^{3+} \rightarrow Ln^{3+}$ energy transfer. The energy transfer efficiency was determined by the following equation:

$$\eta = 1 - \frac{\tau 0}{\tau Ln3+} \quad (4)$$

where τ_0 and τ_{Ln3+} are the Ti^{3+} lifetimes in the absence and presence of the energy acceptor, respectively. Usually, the τ_0 is determined as a lifetime of the energy donor for un-doped systems. However, in the analyzed case for a sample undoped with Ln^{3+} ions, the Ti^{3+} ions are mainly located in the surface layer of the grain, where the probability of non-radiative relaxation of the excited level is high. Therefore, in the analysis carried out, we have used the lifetimes for

$SrTiO_3:Gd^{3+}$ and $CaTiO_3:Gd^{3+}$ samples as τ_0, because the presence of Gd^{3+} ions enables the reduction of the oxidation state of titanium ions and their energy level scheme consists of the energy levels localized only at very high energies preventing the occurrence of $Ti^{3+}\rightarrow La^{3+}$ energy transfer. As can be seen, the energy transfer efficiency for almost all Ln^{3+} ions is very high and reaches about 40–60% for $SrTiO_3:Ln^{3+}$, and only 20–50% for $CaTiO_3:Ln^{3+}$ (Fig. S21). In order to obtain reliable values for relative and absolute sensitivity, an appropriate formula was sought to account the rise in lifetimes observed at low temperatures. For this reason, an empirical equation of the following form was proposed (Eq. 5):

$$\tau(T) = \tau_0 \frac{1 + C_2 e^{-\frac{\Delta E_2}{kT}}}{1 + C_1 e^{-\frac{\Delta E_1}{kT}}} \quad (5)$$

where: τ_0 corresponds to the average lifetime at low temperature, ΔE_1 and ΔE_2 to the activation energy, k is the Boltzmann constant, and C_1 and C_2 are constants. The S_A and S_R of the lifetime-based thermometer were calculated and their thermal dependencies are shown in Figs. S22-S23 and Fig. 4e-f, respectively (maximal values of S_A and S_R are summarized in Table S3). Taking into account the inverse monotonicity of the lifetimes at low temperatures, in order to facilitate the comparison of the maximum S_A and S_R values, the absolute values of the results with two maxima are shown in the plots. For both S_A and S_R, a shift of the maximal values towards higher temperatures was observed for $CaTiO_3$ powders in respect to $SrTiO_3$ powders. Maximal S_A values were obtained for $SrTiO_3:Sm^{3+}$, equal to $S_{Amax} = 717\ \mu sK^{-1}$ at 125 K and for $CaTiO_3:Tb^{3+}$ equal to $666\ \mu sK^{-1}$ at 195 K. In the case of S_{Rmax}, all results exceeded $2\%\ K^{-1}$. The highest results are presented by $SrTiO_3:Dy^{3+}$ with the value of $5.87\%\ K^{-1}$ at 140 K, $SrTiO_3:Yb^{3+}$ with $5.54\%\ K^{-1}$ at 175 K and $SrTiO_3:Sm^{3+}$ with $S_{Rmax} = 5.50\%\ K^{-1}$ at 135 K. For lifetimes of $CaTiO_3:Ln^{3+}$, although the S_R values were lower (up to a maximum of $4.51\%\ K^{-1}$), they were obtained at higher temperatures, which increases their application potential. In this case it is worth noting $S_R = 4.51\%\ K^{-1}$ at 251 K for Gd^{3+}-doped $CaTiO_3$ nanocrystals. The analysis performed reveals that the introduction of Ln^{3+} ions into the $SrTiO_3$ and $CaTiO_3$ brings multifaced benefits to the thermometric performance of a lifetime-based luminescent thermometer exploiting Ti^{3+} emission. First of all, doping with Ln^{3+} due to the charge compensating effect stabilizes the Ti^{3+} state and enhances its emission intensity. Secondly, the relaxation of the radiative transition probability elongates the value of τ_{avr}. This effect is especially favorable since in lifetime-based thermal imaging the intensity ratio captured in the two time gates is usually considered as a thermometric parameter. The time width of a gate is limited by the decay time itself. Therefore, in order to collect a higher emission signal, longer gates and thus lifetimes are desired. Moreover, the modification of the local ions symmetry associated with the presence of Ln^{3+} leads to a modulation of the thermometric performance of the lifetime-based thermometer, including the maximal S_R and the usable temperature range in which given luminescent thermometer can be applied.

4. Conclusions

In this work the thermometric properties of the lifetime-based luminescent thermometers exploiting Ti^{3+} ions emission in $SrTiO_3$ and $CaTiO_3$ were investigated. It was found that the introduction of the Ln^{3+} ions enables to enhance the intensity of $^2E\rightarrow {}^2T_2$ emission band of Ti^{3+} due to the stabilization of the Ti^{3+} states via charge compensation. Stronger distortion of the Ti^{3+} symmetry from the octahedral site observed in $CaTiO_3$ results in a broader emission band of Ti^{3+} ions. The increase of the temperature results in the slight increase of the Ti^{3+} emission intensity up to around 140 K followed by the luminescence thermal quenching in $SrTiO_3$. On the other hand, a more significant initial thermal enhancement of the Ti^{3+} emission band was found for $CaTiO_3:Ln^{3+}$, even up to 1.78 at 183 K of the value recorded at 83 K for $CaTiO_3:Tb^{3+}$. Analogously the average lifetimes of the ^2E state of Ti^{3+} elongate at elevated temperatures up to around 143 K for $SrTiO_3:Ln^{3+}$ and 183 K for $CaTiO_3:Ln^{3+}$ followed by the thermal shortening due to the thermal quenching process. Both increases of the emission intensity and the elongation of the Ti^{3+} lifetime were discussed in terms of the temperature induced increase of the probability of the radiative depopulation of the ^2E state caused by the relaxation of the selection rules associated with the mixing of the wavefunctions of the excited states of Ti^{3+} ions. The most spectacular elongation of the lifetime of the ^2E state was observed for $SrTiO_3:Nd^{3+}$, for which the average lifetime τ_{avr} increased from 4.2 ms at 83 K to as much as 20.7 ms at 115 K. Moreover, it was shown that the relative sensitivity and the usable temperature range within which the relative sensitivity of the luminescent thermometer exceeds $1\%\ K^{-1}$ can be altered by the selection of the Ln^{3+} ion. The maximal values of the lifetime based luminescent thermometers were found to be $S_R = 5.87\%\ K^{-1}$ at 140 K for $SrTiO_3:Dy^{3+}$ and $S_R = 4.51\%\ K^{-1}$ at 251 K for $CaTiO_3:Gd^{3+}$. The multifaced improvement of the thermometric parameters of lifetime based luminescent thermometers by the introduction of the Ln^{3+} ions including the stabilization of the Ti^{3+} oxidation state, the elongation of the lifetime value combined with the modulation of the relative sensitivity and usable temperature range confirms the high potential of the proposed strategy in the development of temperature sensors of predefined thermometric parameters.

CRediT authorship contribution statement

Wojciech M. Piotrowski: Methodology, Investigations, Writing – original draft. **Zoran Ristić:** Methodology, Investigations, Writing – original draft. **Miroslav D. Dramićanin:** Methodology, Investigations, Writing – original draft. **Lukasz Marciniak:** Conceptualization, Methodology, Investigations, Writing – original draft.

Declaration of Competing Interest

The authors declare that they have no known competing financial interests or personal relationships that could have appeared to influence the work reported in this paper.

Acknowledgements

The "High sensitive thermal imaging for biomedical and microelectronic application" project was carried out within the First Team programme of the Foundation for Polish Science cofinanced by the European Union under the European Regional Development Fund.

Appendix A. Supporting information

Supplementary data associated with this article can be found in the online version at doi:10.1016/j.jallcom.2022.164398.

References

[1] D. Jaque, F. Vetrone, Luminescence nanothermometry, Nanoscale 4 (2012) 4301–4326.
[2] C.D.S. Brites, A. Millán, L.D. Carlos, Chapter 281 - Lanthanides in Luminescent Thermometry, in: B. Jean-Claude, P.B.T.-H. on the P., C. of R.E. Vitalij K. (Eds.), Incl. Actinides, Elsevier, 2016, pp. 339–427.
[3] L.Đa.čanin Far, S.R. Lukić-Petrović, V. Đorđević, K. Vuković, E. Glais, B. Viana, M.D. Dramićanin, Luminescence temperature sensing in visible and NIR spectral range using Dy^{3+} and Nd^{3+} doped $YNbO_4$, Sens. Actuators A Phys. 270 (2018) 89–96.
[4] C.D.S. Brites, P.P. Lima, N.J.O. Silva, A. Millán, V.S. Amaral, F. Palacio, L.D. Carlos, Thermometry at the nanoscale, Nanoscale 4 (2012) 4799–4829.

[5] A. Bednarkiewicz, J. Drabik, K. Trejgis, D. Jaque, E. Ximendes, L. Marciniak, Luminescence based temperature bio-imaging: status, challenges, and perspectives, Appl. Phys. Rev. 8 (2021) 11317.

[6] L. Marciniak, A. Bednarkiewicz, D. Kowalska, W. Strek, A new generation of highly sensitive luminescent thermometers operating in the optical window of biological tissues, J. Mater. Chem. C 4 (2016) 5559–5563.

[7] K. Elzbieciak-Piecka, C. Matuszewska, L. Marciniak, Step by step designing of sensitive luminescent nanothermometers based on Cr^{3+},Nd^{3+} co-doped $La_{3-x}Lu_xAl_{5-y}Ga_yO_{12}$ nanocrystals, N. J. Chem. 43 (2019) 12614–12622.

[8] M. Back, J. Ueda, M.G. Brik, T. Lesniewski, M. Grinberg, S. Tanabe, Revisiting Cr^{3+}-Doped $Bi_2Ga_4O_9$ spectroscopy: crystal field effect and optical thermometric behavior of near-infrared-emitting singly-activated phosphors, ACS Appl. Mater. Interfaces 10 (2018) 41512–41524.

[9] M. Back, J. Ueda, J. Xu, D. Murata, M.G. Brik, S. Tanabe, Ratiometric luminescent thermometers with a customized phase-transition-driven fingerprint in perovskite oxides, ACS Appl. Mater. Interfaces 11 (2019) 38937–38945.

[10] Z. Ristić, V. Đorđević, M. Medić, S. Kuzman, M.G. Brik, Ž. Antić, M.D. Dramićanin, Temperature dependence of the Cr^{3+}-doped Mg_2TiO_4 near-infrared emission, Opt. Mater. (Amst.) 120 (2021) 111468.

[11] L. Marciniak, K. Trejgis, Luminescence lifetime thermometry with Mn^{3+}–Mn^{4+} co-doped nanocrystals, J. Mater. Chem. C 6 (2018) 7092–7100.

[12] K. Elzbieciak, A. Bednarkiewicz, L. Marciniak, Temperature sensitivity modulation through crystal field engineering in Ga^{3+} co-doped $Gd_3Al_{5-x}Ga_xO_{12}$:Cr^{3+}, Nd^{3+} nanothermometers, Sens. Actuators B Chem. 269 (2018) 96–102.

[13] S.A. Wade, S.F. Collins, G.W. Baxter, Fluorescence intensity ratio technique for optical fiber point temperature sensing, J. Appl. Phys. 94 (2003) 4743–4756.

[14] F. Shang, C. Hu, W. Xu, L. Zhao, S. Zong, M. Yao, F. Bai, Z. Zhang, Modulation of luminescence thermometry in Nd^{3+}-Yb^{3+} co-activated phosphors via engineering host matrix, J. Alloy. Compd. 896 (2022) 162794.

[15] K. He, L. Zhang, Y. Liu, B. Xu, L. Chen, G. Bai, Lanthanide ions doped nonhygroscopic $La_2Mo_3O_{12}$ microcrystals based on multimode luminescence for optical thermometry, J. Alloy. Compd. 890 (2022) 161918.

[16] N. Zhang, H. Zhou, Y. Yin, T. Wang, J. Zhang, L. Ye, Z. Jia, X. Tao, Exploring promising up-conversion luminescence single crystal fiber in sesquioxide family for high temperature optical thermometry application, J. Alloy. Compd. 889 (2021) 161348.

[17] T. Zheng, M. Runowski, N. Stopikowska, M. Skwierczyńska, S. Lis, P. Du, L. Luo, Dual-center thermochromic Bi_2MoO_6:Yb^{3+}, Er^{3+}, Tm^{3+} phosphors for ultrasensitive luminescence thermometry, J. Alloy. Compd. 890 (2022) 161830.

[18] K. Saidi, M. Dammak, K. Soler-Carracedo, I.R. Martín, Optical thermometry based on upconversion emissions in $Na_3Gd(VO_4)_2$: Yb^{3+}-Er^{3+}/Ho^{3+} micro crystals, J. Alloy. Compd. 891 (2022) 161993.

[19] P.R.N. Childs, J.R. Greenwood, C.A. Long, Review of temperature measurement, Rev. Sci. Instrum. 71 (2000) 2959–2978.

[20] M.D. Dramićanin, Trends in luminescence thermometry, J. Appl. Phys. 128 (2020) 40902.

[21] M.G. Brik, Ab-initio studies of the electronic and optical properties of Al_2O_3:Ti^{3+} laser crystals, Phys. B Condens. Matter 532 (2018) 178–183.

[22] L.M.B. Hickey, E. Martins, J.E. Román, W.S. Brocklesby, J.S. Wilkinson, Fluorescence of Ti^{3+} ions thermally diffused into sapphire, Opt. Lett. 21 (1996) 597–599.

[23] M.G. Brik, N.M. Avram, C.N. Avram, N.M. Avram, M.G. Brik (Eds.), Exchange charge model of crystal field for 3d ions BT - Optical Properties of 3d-Ions in Crystals: Spectroscopy and Crystal Field Analysis, Springer Berlin Heidelberg, Berlin, Heidelberg, 2013, pp. 29–94.

[24] J. Drabik, B. Cichy, L. Marciniak, New type of nanocrystalline luminescent thermometers based on Ti^{3+}/Ti^{4+} and Ti^{4+}/Ln^{3+} (Ln^{3+} = Nd^{3+}, Eu^{3+}, Dy^{3+}) luminescence intensity ratio, J. Phys. Chem. C 122 (2018) 14928–14936.

[25] J. Drabik, L. Marciniak, The influence of Eu^{3+} concentration on the spectroscopic properties of YAG:Ti, Eu^{3+} nanocrystalline luminescent thermometer, J. Lumin. 208 (2019) 213–217.

[26] W. Piotrowski, M. Kuchowicz, M. Dramićanin, L. Marciniak, Lanthanide dopant stabilized Ti^{3+} state and supersensitive Ti^{3+} -based multiparametric luminescent thermometer in $SrTiO_3$:Ln^{3+} (Ln^{3+} = Lu^{3+}, La^{3+}, Tb^{3+}) nanocrystals, Chem. Eng. J. 428 (2022) 131165.

[27] M. Johnsson, P. Lemmens, Crystallography and chemistry of perovskites, Handb. Magn. Adv. Magn. Mater. (2007).

[28] C.J. Ball, B.D. Begg, D.J. Cookson, G.J. Thorogood, E.R. Vance, Structures in the system $CaTiO_3$/$SrTiO_3$, J. Solid State Chem. 139 (1998) 238–247.

[29] A. Boudali, A. Abada, M. Driss Khodja, B. Amrani, K. Amara, F. Driss Khodja, A. Elias, Calculation of structural, elastic, electronic, and thermal properties of orthorhombic $CaTiO_3$, Phys. B Condens. Matter 405 (2010) 3879–3884.

[30] P.J. Dereń, R. Mahiou, R. Pązik, K. Lemanski, W. Stręk, P. Boutinaud, Upconversion emission in $CaTiO_3$:Er^{3+} nanocrystals, J. Lumin. 128 (2008) 797–799.

[31] M. Yashima, R. Ali, Structural phase transition and octahedral tilting in the calcium titanate perovskite $CaTiO_3$, Solid State Ion. 180 (2009) 120–126.

[32] R. Ali, M. Yashima, Space group and crystal structure of the perovskite $CaTiO_3$ from 296 to 1720K, J. Solid State Chem. 178 (2005) 2867–2872.

[33] V. Đorđević, M.G. Brik, A.M. Srivastava, M. Medić, P. Vulić, E. Glais, B. Viana, M.D. Dramićanin, Luminescence of Mn^{4+} ions in $CaTiO_3$ and $MgTiO_3$ perovskites: Relationship of experimental spectroscopic data and crystal field calculations, Opt. Mater. (Amst.) 74 (2017) 46–51.

[34] T. Kubo, H. Nozoye, Surface structure of $SrTiO_3$(100), Surf. Sci. 542 (2003) 177–191.

[35] V.M. Goldschmidt, Die Gesetze der Krystallochemie, Naturwissenschaften 14 (1926) 477–485.

[36] P. Woodward, Octahedral tilting in Perovskites. II. structure stabilizing forces, Acta Crystallogr. Sect. B 53 (1997) 44–66.

[37] A. Sandhyarani, M.K. Kokila, G.P. Darshan, H. Nagabhushana, S.C. Sharma, H.B. Premkumar, D. Prasad, Fabrication of flux supported $SrTiO_3$:Eu^{3+} fluorescent powders: new prospective of dual mode, ink-free data security applications, J. Sci. Adv. Mater. Devices 6 (2021), pp. 92–99.

[38] D. Gao, X. Zhang, J. Zhang, The effects of structural characterization on the luminescence of Eu^{3+}-doped fluoride nano/microcrystals, CrystEngComm 16 (2014) 11115–11121.

[39] X. Zhang, M. Wang, J. Ding, D. Gao, Y. Shi, X. Song, The novel upconversion properties of $LiYbF_4$:Er microcrystals compared to the Na counterpart, CrystEngComm 14 (2012) 8357–8360.

[40] S. Tsunekawa, H.F.J. Watanabe, H. Takei, Linear thermal expansion of $SrTiO_3$, Phys. Status Solidi 83 (1984) 467–472.

[41] T. Tadano, S. Tsuneyuki, Ab initio prediction of structural phase-transition temperature of $SrTiO_3$ from finite-temperature phonon calculation, J. Ceram. Soc. Jpn. 127 (2019) 404–408.

[42] R.O. Bell, G. Rupprecht, Elastic constants of strontium titanate, Phys. Rev. 129 (1963) 90–94.

[43] R.A. Cowley, W.J.L. Buyers, G. Dolling, Relationship of normal modes of vibration of strontium titanate and its antiferroelectric phase transition at 110°K, Solid State Commun. 7 (1969) 181–184.

[44] G. Shirane, Y. Yamada, Lattice-dynamical study of the 110K phase transition in $SrTiO_3$, Phys. Rev. 177 (1969) 858–863.

[45] P.A. Fleury, J.F. Scott, J.M. Worlock, Soft phonon modes and the 110K phase transition in $SrTiO_3$, Phys. Rev. Lett. 21 (1968) 16–19.

[46] D.A. Tenne, A.K. Farrar, C.M. Brooks, T. Heeg, J. Schubert, H.W. Jang, C.W. Bark, C.M. Folkman, C.B. Eom, D.G. Schlom, Ferroelectricity in nonstoichiometric $SrTiO_3$ films studied by ultraviolet Raman spectroscopy, Appl. Phys. Lett. 97 (2010) 142901.

[47] A.A. Sirenko, I.A. Akimov, J.R. Fox, A.M. Clark, H.-C. Li, W. Si, X.X. Xi, Observation of the first-order raman scattering in $SrTiO_3$ thin films, Phys. Rev. Lett. 82 (1999) 4500–4503.

[48] S.A.T. Redfern, High-temperature structural phase transitions in perovskite, J. Phys. Condens. Matter 8 (1996) 8267–8275.

[49] B.J. Kennedy, C.J. Howard, B.C. Chakoumakos, Phase transitions in perovskite at elevated temperatures - a powder neutron diffraction study, J. Phys. Condens. Matter 11 (1999) 1479–1488.

[50] H. Gränicher, O. Jakits, Über die dielektrischen Eigenschaften und Phasenumwandlungen bei Mischkristallsystemen vom Perowskittyp, Nuovo Cim. 11 (1954) 480–520.

[51] N.Z. Koocher, L.-F. Huang, J.M. Rondinelli, Negative thermal expansion in the Ruddlesden-Popper calcium titanates, Phys. Rev. Mater. 5 (2021) 53601.

[52] K.S. Knight, Structural and thermoelastic properties of $CaTiO_3$ perovskite between 7K and 400K, J. Alloy. Compd. 509 (2011) 6337–6345.

[53] F. Shi, G. Fu, E.-C. Xiao, J. Li, Lattice vibrational characteristics and dielectric properties of pure phase $CaTiO_3$ ceramic, J. Mater. Sci. Mater. Electron. 31 (2020) 18070–18076.

[54] G. Dong, X. Xiao, L. Zhang, Z. Ma, X. Bao, M. Peng, Q. Zhang, J. Qiu, Preparation and optical properties of red, green and blue afterglow electrospun nanofibers, J. Mater. Chem. 21 (2011) 2194–2203.

[55] Y. Li, S. Qin, F. Seifert, Phase transitions in A-site substituted perovskite compounds: the $(Ca_{1-2x}Na_xLa_x)TiO_3$ ($0 \le x \le 0.5$) solid solution, J. Solid State Chem. 180 (2007) 824–833.

[56] Y. Tanabe, S. Sugano, On the absorption spectra of complex ions. I, J. Phys. Soc. Jpn. 9 (1954) 753–766.

[57] Y. Tanabe, H. Kamimura, On the absorption spectra of complex ions IV. the effect of the spin-orbit interaction and the field of lower symmetry on d electrons in cubic field, J. Phys. Soc. Jpn. 13 (1958) 394–411.

[58] M.G. Brik, N.M. Avram, Microscopic analysis of the crystal field strength and electron-vibrational interaction in cubic $SrTiO_3$ doped with Cr^{3+}, Mn^{4+} and Fe^{5+} ions, J. Phys. Condens. Matter 21 (2009) 155502.

[59] A. Bednarkiewicz, L. Marciniak, L.D. Carlos, D. Jaque, Standardizing luminescence nanothermometry for biomedical applications, Nanoscale 12 (2020) 14405–14421.

[60] M. Grinberg, J. Barzowska, Y.R. Shen, K.L. Bray, J. Hanuza, P.J. Dereń, The effect of pressure on luminescence properties of Cr^{3+} ions in $LiSc(WO_4)_2$ crystals—Part II: pressure- and temperature-dependent luminescence kinetics, J. Lumin. 116 (2006) 15–27.

[61] M. Grinberg, T. Lesniewski, S. Mahlik, R.S. Liu, $3d^3$ system – comparison of Mn^{4+} and Cr^{3+} in different lattices, Opt. Mater. (Amst.) 74 (2017) 93–100.